J. Appl. Cryst. (1994). **27**, 1020–1029

Small-Angle Neutron Scattering Study of Dislocations in Deformed Single-Crystal Copper

BY BRENT J. HEUSER*

University of Missouri Research Reactor Center and Department of Physics and Astronomy, Columbia, MO 65211, USA

(*Received* 30 *December* 1993; *accepted* 18 *July* 1994)

Abstract

Small-angle neutron scattering measurements of deformed single-crystal copper have been performed over a wave-vector transfer range of $0.0655 \leq Q \leq 1.32\,\text{nm}^{-1}$. The measurements included four samples deformed in compression at room temperature along the [110] direction to 6.8, 15.6, 35.0 and 54.3% reduction in thickness and an undeformed reference sample. The response of the reference sample followed the Porod law at lowest Q and was, at least in part, the result of scattering from the external surfaces of the sample. The radially averaged net cross sections were found to increase with increasing deformation, while the power-law exponent n ($\mathrm{d}\Sigma/\mathrm{d}\Omega \propto 1/Q^n$) decreased from $n \simeq 3$ to $n \simeq 2.2$ with increasing deformation. The scattering response of the two most deformed samples was noticeably anisotropic. Analysis of this anisotropy revealed strong $1/Q^2$ scattering perpendicular to the {111} dislocation slip planes, in agreement with the theoretical work of Seeger [*J. Appl. Phys.* (1959), **30**, 629–637]. The decrease in the *radially averaged* power-law exponent is therefore attributed to strong $1/Q^2$ behavior at the highest levels of deformation. Bulk-averaged edge dislocation densities that varied systematically from approximately 1×10^{10} to $5 \times 10^{10}\,\text{cm}^{-2}$ were obtained from the measured data.

Introduction

Neutron scattering measurements of deformed metals have an important historical significance – one of the first small-angle neutron scattering (SANS) experiments performed was the study of dislocations in copper and aluminium by Atkinson (1959). These experiments were motivated by inconsistencies between the predicted scattering behavior from dislocations and measured X-ray intensities from deformed metals, which were evidently contaminated by multiple Bragg diffraction. In support of these early X-ray and neutron measurements, theoretical descriptions from, for example, isolated dislocations (Atkinson & Hirsch, 1958) and dislocation arrays (Seeger, 1959), were abundant in the 1950s.

Theoretical endeavors in this area quickly gained a level of sophistication that was unmatched by any neutron experiment for at least a decade. While the initial experiments by Atkinson did succeed in verifying the expected magnitude of the neutron scattering cross section from dislocations in a deformed metal matrix, the experimental arrangement did not allow for accurate measurements of intensity as a function of scattering angle. Some progress was made when Christ (1964) observed a small-angle scattering intensity from deformed polycrystalline copper (with the intensity from an undeformed reference sample subtracted) that was inversely proportional to the third power of the scattering angle. This result, over a somewhat limited scattering-angle range, agreed with the behavior predicted by Atkinson & Hirsch (1958) for the orientation average of an isolated dislocation.

Christ also observed fall-off in intensity from the expected $1/\theta^3$ behavior at smallest scattering angles and attributed this to an interference effect. This explanation is debatable, however, given the strong forward scattering response of the undeformed reference sample. In fact, the intensity from the reference sample had a scattering-angle dependence that was quite similar to that of the deformed sample.

Of special relevance to the measurements presented here is the deformed copper single-crystal measurement by Christ (1964). A dramatic anisotropy in the scattered intensity was observed when the neutron wave-vector direction was changed relative to an activated dislocation glide plane. Although the angular distribution of the intensity was not determined, this measurement did confirm, at least qualitatively, the theoretical work of Seeger (1959). Seeger developed a formalism in which the dislocation orientation is represented in a dislocation density tensor. The azimuthal dependence of the scattering cross section is then given by the vector product $(\mathbf{b} \times \mathbf{Q}) \cdot \mathbf{l}$, where $\mathbf{b}$ is the Burgers vector, $\mathbf{Q}$ is the wave-vector transfer with magnitude $Q = (4\pi/\lambda)\sin\theta/2$, λ is the neutron wavelength, θ is the scattering angle and $\mathbf{l}$ is the dislocation line direction. Seeger (1959) predicted a $1/Q^2$ cross-sectional dependence when Q is perpendicular to an activated edge dislocation glide plane.

The azimuthal behavior of dislocation scattering in deformed single-crystal copper, nickel and iron was in-

* Present address: University of Illinois, Department of Nuclear Engineering, 214 Nuclear Engineering Laboratory, 103 South Goodwin Avenue, Urbana, IL 61801-2984, USA.

vestigated more completely in measurements performed on the Dll instrument in Grenoble, France, during the 1970s. This work is summarized in review articles by Schmatz (1975) and Gerold & Kostorz (1978). While the $(\mathbf{b} \times \mathbf{Q}) \cdot \mathbf{l}$ asymmetry predicted by Seeger was verified, the preferred-orientation $1/Q^2$ behavior and the orientation-average $1/Q^3$ behavior were not (Schmatz, 1975; Gerold & Kostorz, 1978).

More recently, SANS measurements of fatigued single-crystal copper have been performed by Kettunen, Lepistö, Kostorz & Göltz (1981) and by Lepistö, Kostorz, Kuokkala & Kettunen (1991). These experiments were designed to monitor void formation induced by cyclic deformation, but sensitivity to dislocation generation existed as well. It must be realized, though, that information regarding dislocation scattering extracted from these data is done so under nonideal conditions. This is because the void and dislocation scattering responses must be separated and analyzed individually. This task is further complicated by the fact that two different void SANS responses, one Guinier-like and one Porod-like, can be observed, depending on the void size and Q range of the measurement (see, for example, Lepistö, Kostorz, Kuokkala & Kettunen, 1991).

Lepistö *et al.* (1991) observed residual dislocation scattering in fatigued single-crystal copper after subtraction of a Guinier-like void response and an incoherent background term. This residual dislocation scattering followed the $1/Q^3$ behavior expected for an orientation average of the edge dislocation strain field. Anisotropic scattering was not observed in this study but, as the authors note, the samples were not oriented in a configuration favorable to the detection of an asymmetric dislocation response. Edge dislocation densities of approximately 4×10^{10} cm^{-2} were determined from a fit of residual $1/Q^3$ behavior of the most heavily fatigued samples.

The work of Kettunen *et al.* (1981) is less explicit in the treatment of dislocation scattering. Although the samples were oriented with a [111] direction contained in the measured Q plane, anisotropic scattering was not observed. The statistical errors were quite large in this work, however, and the lack of an asymmetric scattering pattern is not meaningful. The incremental SANS response of a sample fatigued to 80% of its expected life to that of a 20% fatigued sample was modeled with a Guinier-like void response and a $1/Q^3$ edge dislocation response. The edge dislocation density obtained from this fitting procedure was 4×10^{10} cm^{-2}.

SANS measurements of single-crystal copper deformed in compression to various degrees of thickness reduction are presented below. The purpose of the measurements was twofold: first, to study the dislocation scattering behavior as a function of deformation; second, to analyze the azimuthal dependence of the SANS response. It is shown below that the radially averaged net cross sections (differences between deformed sample and undeformed reference sample) increase in magnitude with increasing deformation, while the power-law exponent n ($\mathrm{d}\Sigma/\mathrm{d}\Omega \propto 1/Q^n$) decreases from $n \simeq 3$ to $n \simeq 2.2$ with increasing deformation. The latter observation could be construed as evidence of an interference effect dominating at the larger amounts of deformation. However, analysis of the azimuthal dependence demonstrates that this change is the result of increasing $1/Q^2$ scattering in directions perpendicular to {111} slip planes of the more heavily deformed single-crystal samples.

Experimental procedures used for sample preparation and SANS investigation are presented in the next section. A review of dislocation scattering theory is given. SANS results are presented and discussed in the final section.

Experimental

Four deformed samples were prepared from a 99.999% pure single-crystal copper ingot with a [110] cylinder axis grown by Metron, Inc. This ingot had a starting length of 3.8 cm and a starting diameter of 1.3 cm. Four pieces were cut from the ingot with a low-speed diamond saw and deformed in compression between two lubricated steel plates. The four deformed samples were compressed at room temperature in the [110] cylinder direction to 6.8, 15.6, 35.0 and 54.3% reduction in thickness (the percentage reduction is the ratio of the change in thickness to the initial thickness) and are referred to as Cu7, Cu16, Cu35 and Cu54, respectively. An as-grown undeformed reference sample was also cut from the ingot and is referred to as CuREF.

The samples were mechanically polished, with 0.05 μm aluminium oxide used in the final step, to remove surface irregularities and impurities introduced during cutting and deformation. The polished faces of all the samples were (110), with the direction of deformation perpendicular to these faces. The SANS measurement geometry was such that the incident beam was normal to the sample face (parallel to the original direction of deformation). The final thickness of each sample was approximately 0.5 cm, except for Cu54, which had a final thickness of 0.35 cm.

The SANS measurements were performed at the NIST-CNRF using the 30 m NSF instrument (Hammouda, Krueger & Glinka, 1993). All samples were measured in a vacuum at room temperature with the instrument in two resolution configurations. To probe the intermediate wave-vector transfer range of $0.153 \leq Q \leq 1.32$ nm^{-1}, the instrument configuration was as follows: source-to-sample distance 392 cm, sample-to-detector distance 300 cm, beam-stop diameter 7.62 cm, sample aperture 1.03 cm, source aperture 5 cm and neutron wavelength 0.720 ± 0.247 nm (±FWHM). This

Table 1. *Integrated counting rates over detector* (s^{-1})

	Intermediate-Q configuration	Low-Q configuration
Beam-blocked background	5.2	3.3
Open beam	12.1	5.2
CuREF	31.7	5.7
Cu7	32.1	5.9
Cu16	33.2	6.2
Cu35	35.0	7.0
Cu54	35.3	8.0

instrumental setting is referred to as the intermediate-Q configuration. The low-Q configuration, which probed the wave-vector transfer range $0.0655 \leq Q \leq 0.576\,\mathrm{nm}^{-1}$, was obtained by changing the source-to-sample distance to 857 cm and the sample-to-detector distance to 700 cm while holding all other parameters fixed. The integrated counting rates over the entire 64×64 cm detector are given in Table 1.

The data were taken by cycling the five copper samples, an empty-beam configuration and a beam-blocked configuration on an automatic sample translator. Each position was periodically moved into the incident beam for 1 to 2 h, with Cu35 and Cu54 counted for shorter times. All measurements were then corrected for sample transmission, empty-beam and beam-blocked backgrounds and relative pixel-to-pixel detector sensitivity. The complete experiment (both Q configurations) was performed over a 96 h period.

The intermediate Q data for each sample were placed on an absolute scale by calibrating against the scattering response from 0.1 cm of water. The low-Q data were then scaled to the intermediate cross sections over a common data range of $0.15 \leq Q \leq 0.5\,\mathrm{nm}^{-1}$. This overlap region consisted of 25 data points from the intermediate-Q configuration and 60 data points from the low-Q configuration. All SANS measurements presented below are given as macroscopic differential cross sections.

Data are presented below both as radial averages over the entire detector and as sector averages over pie-shaped regions of the detector. In all cases, a binning width of 1 cm perpendicular to $\mathbf{Q}$ was used in the data reduction.

Theoretical framework

The derivation of the differential macroscopic cross section per steradian describing the scattering response from dislocation arrays is reviewed in this section. This derivation follows the work of Seeger (1959). First, the differential scattering cross section from an isolated edge dislocation is given by

$$\mathrm{d}\Sigma(\mathbf{Q})/\mathrm{d}\Omega = \left(a^2/4\pi V\kappa^2\right)\left|\int_V \Theta(\mathbf{r})\exp\left(i\mathbf{Q}\cdot\mathbf{r}\right)\mathrm{d}\mathbf{r}\right|^2. \tag{1}$$

In (1), a is the bound-atom coherent scattering length of copper, V is the sample volume exposed to the neutron beam, κ is the atomic volume of copper, $\Theta(\mathbf{r})$ is the local volume dilatation, $\Delta V/V$, of the dislocation, $\mathbf{Q}$ is the neutron wave-vector transfer vector and $\mathbf{r}$ is the position vector.

At this point, the cross section can be determined by substituting the functional form of $\Theta(\mathbf{r})$ into (1). Following this procedure, Atkinson & Hirsch (1958) derived a $\mathrm{d}\Sigma/\mathrm{d}\Omega \propto 1/Q^3$ scattering behavior for the orientation average of an isolated edge dislocation. This result is applicable for Q values such that $QR > 4$, where R is the mean dislocation spacing, while interference effects between nearby dislocations are expected to dominate at smaller Q (Atkinson & Hirsch, 1958).

Seeger (1959) employed a different methodology that explicitly accounted for the dislocation arrangement on the glide plane. By the definition of a continuous dislocation-density tensor, α, the scattering cross section can be written as

$$\mathrm{d}\Sigma(\mathbf{Q})/\mathrm{d}\Omega = \left[(1-2\nu)/(1-\nu)\right]^2\left(a^2/4\pi V\kappa^2\right) \times \left|\int_V \left[\mathrm{tr}\,(\alpha\times\mathbf{Q})/Q^2\right]\exp\left(i\mathbf{Q}\cdot\mathbf{r}\right)\mathrm{d}\mathbf{r}\right|^2, \tag{2}$$

where ν is Poisson's ratio, $\alpha = \mathbf{l}\delta(y)D(x,L^*)\mathbf{b}$, $\delta(y)$ is the Dirac delta function, y is the distance above the glide plane and $D(x,L^*)$ is the density distribution of n_o like-signed dislocations between two obstacles located at $x = \pm L^*/2$. The density distribution is given by $D(x,L^*) = n_o/\{\pi^2[(L^*/2)-x^2]\}^{1/2}$ (Seeger, 1959; Hirth & Lothe, 1982).

Equation (2) can be reduced to the following line integral (Seeger, 1959):

$$\mathrm{d}\Sigma(\mathbf{Q})/\mathrm{d}\Omega = \left[(1-2\nu)/(1-\nu)\right]^2 \times \left(a^2/4\pi V\kappa^2\right)\left[(\mathbf{b}\times\mathbf{Q})/Q^2\right]^2 \cdot \left|\int_{\mathrm{dislocation}} \exp\left(i\mathbf{Q}\cdot\mathbf{r}\right)\mathrm{d}\mathbf{l}\right|^2. \tag{3}$$

Performance of this integration for edge dislocation geometry (Fig. 1) leads to the following scattering cross section (Seeger, 1959):

$$\mathrm{d}\Sigma(Q)/\mathrm{d}\Omega = \left[(1-2\nu)/(1-\nu)\right]^2\left(a^2/4\pi V\kappa^2\right) \times \left[(bL_0n_0)/Q\right]^2\sin^2\varphi\sin^2\tau \times \left\{\sin\left[Q(L_0/2)\cos\tau\right]\right\}^2 \times \left\{J_0\left[Q\sin\tau(L^*/2)\cos\varphi\right]\right\}^2 \times \left[Q(L_0/2)\cos\tau\right]^{-2}, \tag{4}$$

where L_0 is the mean length of straight edge dislocation segments, J_0 is the zeroth-order Bessel function of the first kind, φ is the angle between the projection of $\mathbf{Q}$ onto the xy plane, $\mathbf{Q_r}$, and the x axis, and τ is the angle between $\mathbf{Q}$ and the z axis.

In principle, (4) contains all the functional dependencies of the dislocation SANS response: an orientation average of the dislocation scattering response is given by an integration over all φ and τ, while in the limit as both φ and τ approach 90° (that is, as $\mathbf{Q}$ becomes aligned perpendicular to the dislocation glide plane defined by the Burgers vector, $\mathbf{b}$, and the dislocation line, $\mathbf{l}$, in Fig. 1), $d\Sigma/d\Omega \propto 1/Q^2$. The scattering behavior predicted by numerical integration of (4) is compared to the measured data in the next section.

Results and discussion

(a) *Measured SANS cross sections*

The radially averaged absolute cross sections from the four deformed single-crystal samples and the undeformed reference sample are shown in Fig. 2. (Error limits in all figures and tables represent one standard deviation.) This figure contains low-Q data in linear–linear format. Notice that significant scattering is present at lowest Q in the reference sample measurement. This scattering is shown in better detail in Fig. 3, which gives the low-Q data for CuREF. The scattering response can be fitted very well with the Porod (1982) approximation plus an incoherent term

$$d\Sigma(Q)/d\Omega = (2\pi a^2 N^2/Q^4)(A/V) + d\Sigma/d\Omega_{\text{incoherent}}, \quad (5)$$

where N is the atomic density of copper and A/V is the surface-area-to-volume ratio of the defects resulting in the Porod behavior. A surface-area-to-volume ratio of $0.22\,\text{cm}^{-1}$ is found from a best fit of (5) to the CuREF data. This low-Q Porod behavior is, at least in part, the result of scattering from the scratched surfaces of the sample.

A in (5) represents only that surface area, either internal or external, orthogonal to $\mathbf{Q}$. It follows that no Porod scattering should be observed from an ideally smooth flat external surface aligned perpendicular to the incident-beam direction. However, the samples did not have perfectly smooth surfaces. A uniform array of scratches was present after the final mechanical polishing step. By coincidence, the scratch arrays on each side of CuREF were parallel to within 20°. Two orthogonal sector averages are also shown in Fig. 3, one parallel and the other perpendicular to the known scratch direction. As expected, the two sector averages differ significantly in magnitude, with the sector average perpendicular to the scratches having the largest cross section.

The anisotropic scattering from the polished sample surfaces is problematic. Analysis of the dislocation scattering response, which is also anisotropic, must properly

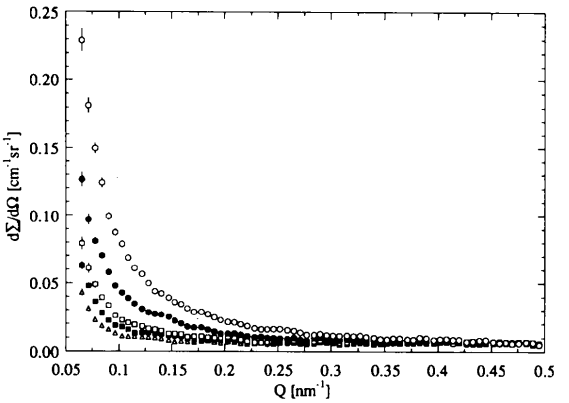

Fig. 2. Radially averaged SANS response of the four deformed samples and one reference sample measured in the low-Q configuration. Curves are for Cu54 (open circles), Cu35 (solid circles), Cu16 (open boxes), Cu7 (solid boxes) and CuREF (open triangles).

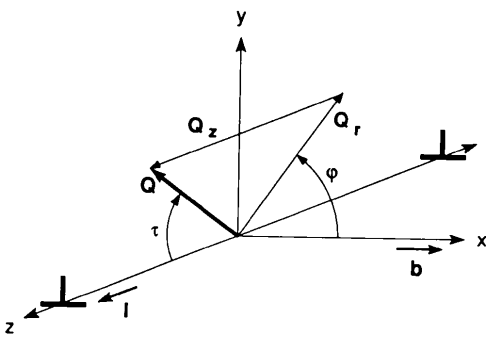

Fig. 1. Edge dislocation glide-plane geometry for the integration given by (3). $\mathbf{Q_r}$ is the projection of $\mathbf{Q}$ onto the xy plane, $\mathbf{Q_z}$ is the projection of $\mathbf{Q}$ onto the xz glide plane, $\mathbf{b}$ is the Burgers vector and $\mathbf{l}$ is a unit vector in the direction of the dislocation line, φ is the angle between $\mathbf{Q_r}$ and $\mathbf{b}$ and τ is the angle between $\mathbf{Q}$ and $\mathbf{l}$. $\mathbf{b}$ and $\mathbf{l}$ are parallel to the x and z axes, respectively

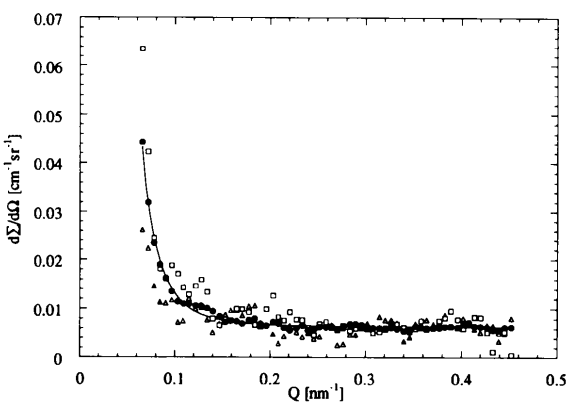

Fig. 3. Radially averaged (solid circles), and sector average perpendicular (open boxes) and parallel (open triangles) to the scratch direction for CuREF. The solid line is a fit of (5) to radially averaged data.

account for the anisotropic surface scattering. Unfortunately, the anisotropic nature of the surface scattering was not anticipated and no effort was made to maintain a consistent scratch direction from sample to sample during polishing or SANS investigation. In all data presented below, the net scattering response is determined by subtracting the *radially averaged* CuREF cross section as a function of Q. This procedure is entirely correct when radially averaged net cross sections are considered. Possible errors that may result when sector averages are analyzed are discussed on a sample-by-sample basis below.

The radially averaged net scattering cross sections of the four deformed samples measured in the low- and intermediate-Q configurations are shown in Figs. 4 and 5, respectively. The net cross sections are plotted in log–log format over a Q range of $0.0655 \leq Q \leq 0.122\,\mathrm{nm}^{-1}$ in Fig. 6. The power-law exponents from Fig. 6, along with cross-sectional values at $Q = 0.0655\,\mathrm{nm}^{-1}$, are given in Table 2.

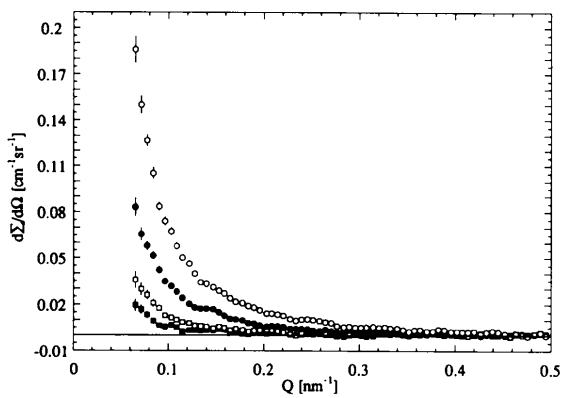

Fig. 4. Radially averaged net scattering response at low Q for Cu54 (open circles), Cu35 (solid circles), Cu16 (open boxes) and Cu7 (solid boxes).

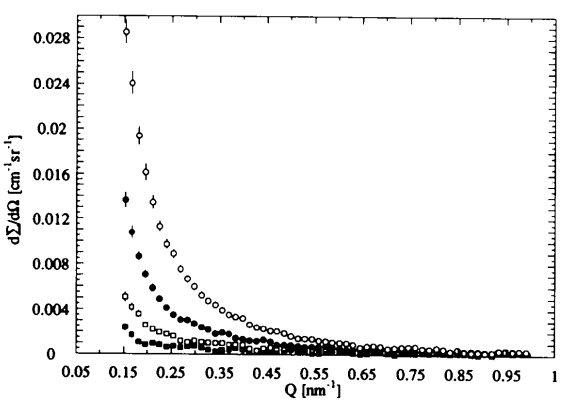

Fig. 5. Radially averaged net scattering response at intermediate Q for Cu54 (open circles), Cu35 (solid circles), Cu16 (open boxes) and Cu7 (solid boxes).

Table 2. *Deformed single-crystal copper net SANS characteristics*

Sample	Power-law exponent n	$d\Sigma/d\Omega$ at $Q = 0.0655\,\mathrm{nm}^{-1}$ ($\mathrm{cm}^{-1}\,\mathrm{sr}^{-1}$)
Cu7	−3.2 (3)	0.020 (4)
Cu16	−2.6 (1)	0.036 (6)
Cu35	−2.20 (6)	0.083 (6)
Cu54	−2.27 (5)	0.186 (9)

There are two trends evident in the scattering characteristics presented in Table 2. First, the low-Q scattering behavior of Cu7 agrees with that expected from an orientation average of an isolated dislocation. As the amount of deformation increases, the scattering response systematically approaches a $d\Sigma/d\Omega \propto 1/Q^2$ behavior. At the same time, the scattering magnitude increases roughly in proportion to the degree of thickness reduction.

At first glance, the reduction in n at low Q might be attributed to an interference effect – an effect that begins to dominate the observed scattering response as the dislocation density increases. This explanation is doubtful though. As demonstrated in Fig. 7, the observed scattering response of Cu54 and Cu35 extends to much higher Q without a change in slope. If an interference effect were present, it would not affect the observed behavior over a full decade of Q, and some type of slope variation should be evident. As discussed below, the scattering responses from the most heavily deformed samples are anisotropic. The systematic variation of the power-law exponent with deformation can be understood by analyzing this anisotropy.

(*b*) *Sector-average analysis*

The anisotropic nature of the dislocation scattering is shown by two sector averages from the net Cu54

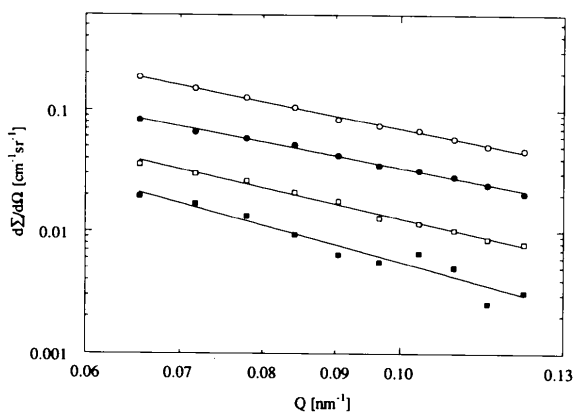

Fig. 6. Radially averaged net scattering cross section at low Q for Cu54 (open circles), Cu35 (solid circles), Cu16 (open boxes) and Cu7 (solid boxes) in log–log format. Solid lines represent linear best fits to data with the power-law exponents given in Table 2.

low-Q measurement in Fig. 8. Iso-intensity contours of this measurement are shown in the inset to Fig. 8. One sector average is over a $\pm 10°$ interval (in the plane of the detector) about a [111] crystallographic direction of the sample and follows a $d\Sigma/d\Omega \propto 1/Q^2$ behavior. The other is over a similar interval about a [227] low-symmetry direction and exhibits a $d\Sigma/d\Omega \propto 1/Q^3$ response. Thus, the scattering response in the Q direction perpendicular to the (111) dislocation glide plane agrees with the behavior predicted by (4) when φ and τ are both equal to 90°. In effect, the scattering shows a 'resonance' under this preferred alignment and the $1/Q^2$ behavior dominates. On the other hand, behavior expected from an orientation average is observed in the low-symmetry direction. This is consistent with all dislocation slip systems contributing to the measured scattering to some degree, without any glide planes aligned in the resonant orientation perpendicular to **Q**.

This sector-analysis methodology is now extended over 180° for Cu54, Cu35 and Cu16 in Fig. 9. Notice that there are four high-symmetry crystallographic directions contained in the measured Q plane: two $\langle 111 \rangle$ types, one $\langle 110 \rangle$ type and one $\langle 100 \rangle$ type. This is illustrated schematically in Fig. 10. A systematic trend that depends on these directions is now evident; the observed response modulates between a $1/Q^2$ behavior and a $1/Q^3$ behavior as the sector angle varies between high- and low-symmetry directions within the Q plane. This is clearest for the Cu54 and Cu35 measurements. These two samples had radially averaged power-law exponents close to -2 (see Table 2), consistent with the high-symmetry $d\Sigma/d\Omega \propto 1/Q^2$ behavior dominating at low and intermediate Q. Cu16 is also seen to have considerable $1/Q^2$ behavior in Fig. 9. As shown in Table 3, however, the amplitude of this behavior for Cu16 is greatly reduced, consistent with the radially averaged low-Q power-law exponent approaching -3.

The scattering amplitudes of the $1/Q^2$ and $1/Q^3$ behaviors are listed in Table 3. These amplitudes are best fits to sector-averaged data determined from the low-Q configuration. When possible, the amplitudes were calculated by averaging over several sector angles. For example, the two $1/Q^2$ amplitudes for Cu54 are averages of the three sector angles $\pm 10°$ about each $\langle 111 \rangle$ direction. The $1/Q^3$ amplitudes are averages over

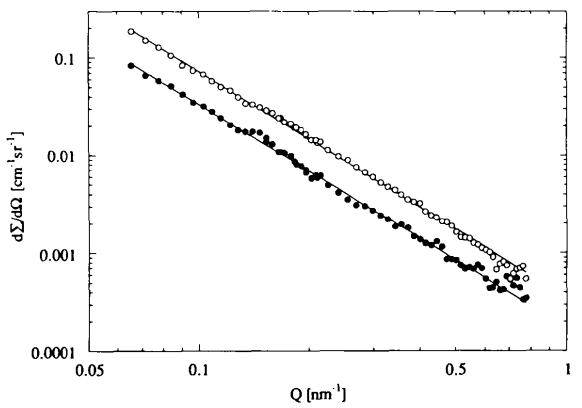

Fig. 7. Radially averaged net scattering response of Cu54 (open circles) and Cu35 (solid circles) over entire Q range in log–log format.

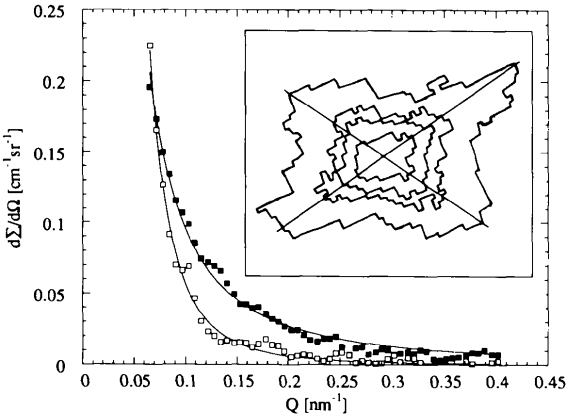

Fig. 8. [111] (solid boxes) and [227] (open boxes) sector averages from the net Cu54 data measured in the low-Q configuration. The solid line through the [111] data is the best fit of $d\Sigma/d\Omega \propto 1/Q^2$. The solid line through the [227] data is the best fit of $d\Sigma/d\Omega \propto 1/Q^3$. The inset shows iso-intensity contours of uncorrected detector response from low-Q Cu54 measurement. The solid lines drawn in the inset correspond to the $\langle 111 \rangle$ crystallographic directions, while the three-o'clock position (zero sector angle) corresponds to a $\langle 110 \rangle$ direction.

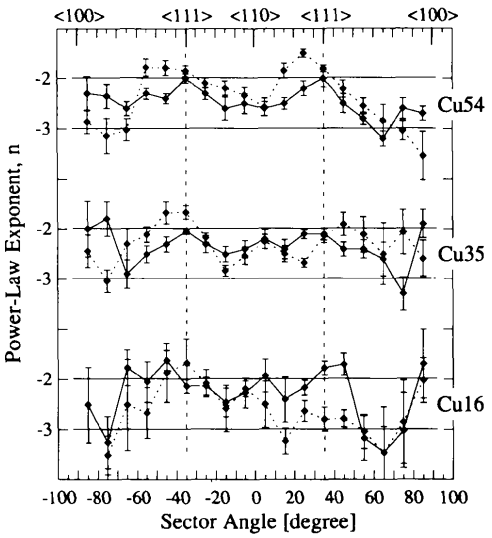

Fig. 9. Power-law exponent, n, as a function of sector angle for the Cu54 (top), Cu35 (middle) and Cu16 (bottom) net measurements in the low-Q (dashed lines) and intermediate-Q (solid lines) configurations. Crystallographic directions contained in the Q plane of measurement are shown at the top of the figure, with two vertical dashed lines at $\pm 35°$ ($\langle 111 \rangle$ directions) drawn as an aid to the eye. The solid horizontal lines denote values of n equal to -2 and -3 for each data set. The Q ranges were $0.07 \leq Q \leq 0.14\ \mathrm{nm}^{-1}$ and $0.17 \leq Q \leq 0.34\ \mathrm{nm}^{-1}$ for low- and intermediate-Q configurations, respectively. The averages were determined over an angular width about each sector angle of $\pm 5°$ for Cu54 and $\pm 15°$ for Cu35 and Cu16.

Table 3. *Scattering amplitudes for resonant and orientation average SANS behaviors*

Sample	$1/Q^2$ amplitude ($\times 10^{-4}$ nm^{-2} cm^{-1} sr^{-1}) +35° ⟨111⟩	$1/Q^2$ amplitude ($\times 10^{-4}$ nm^{-2} cm^{-1} sr^{-1}) −35° ⟨111⟩	$1/Q^3$ amplitude ($\times 10^{-5}$ nm^{-3} cm^{-1} sr^{-1})
Cu7	—	—	0.9 (1) [0.59 (1)]
Cu16	—	1.3 (1)	2.0 (1)
Cu35	3.3 (1)	4.0 (2)	3.2 (1)
Cu54	9.3 (3)	8.4 (3)	5.4 (2)

all off-symmetry directions with n close to -3. The only exception is the additional amplitude given for Cu7, which represents a best fit to the radially averaged $1/Q^3$ result.

The low-Q sector averages for Cu7 and CuREF are given in Fig. 11. Notice that the systematic variation in scattering response is no longer present. In fact, there is a complete lack of $1/Q^2$ behavior in the Cu7 data, consistent with the -3.2 power-law exponent observed at low Q. The CuREF sector-average curve is also consistent with the $1/Q^4$ radially averaged behavior at low Q.

The sector methodology used to analyze the SANS data assumes the observed anisotropy is the result of the nonrandom arrangement of dislocation slip systems in the copper single-crystal lattice. This assumption is reconfirmed by the successful modeling of the measured sector averages with (4) described below. Schmatz, Dederichs & Scheuer (1974), however, have considered copper lattice anisotropy in a theoretical calculation of the edge-dislocation SANS response. For a pure φ rotation ($\tau = 90°$ in Fig. 1), Schmatz *et al.* found the scattered intensity was more strongly peaked toward $\varphi = 90°$ when lattice anisotropy was included in the calculation. [It is important to note that a peak in the intensity at $\varphi = 90°$, resulting from the $(\mathbf{b} \times \mathbf{Q}) \cdot \mathbf{l}$ asymmetry, is present in the isotropic copper lattice calculation as well.] The contribution of lattice anisotropy to the observed modulation in the power-law exponent is therefore difficult to assess, partly because the current measurements do not involve pure φ rotations for all slip systems. Schmatz (1975) has concluded, though, that small-angle scattering from edge dislocations is not significantly affected by the assumption of elastic isotropy.

(c) *Effect of surface scratches*

Some of the data shown in Fig. 9 are affected by the anisotropic scattering from the scratched surfaces of the samples. All the net data in Figs. 9 and 11

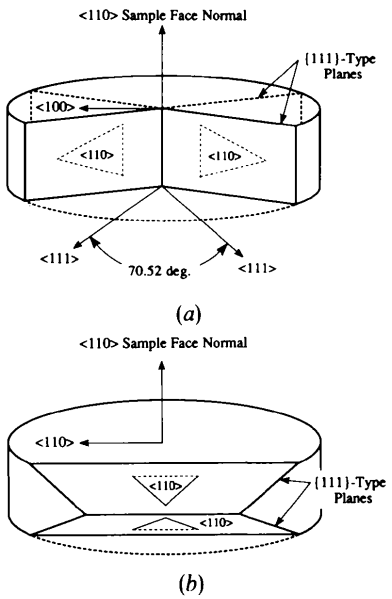

Fig. 10. Orientation of the dislocation slip system geometry with respect to the sample geometry. (*a*) The two {111} slip planes with normal directions in the measured Q plane. (*b*) The two {111} slip planes with normal directions not in the measured Q plane. The three ⟨110⟩ slip directions on each plane are shown as closed triangles. Slip systems with vanishing Schmid factors are shown with dashed slip directions. The samples were deformed in compression along the ⟨110⟩ face normal. SANS measurements were performed with the incident beam perpendicular to the sample face. The measured Q plane is therefore parallel to the sample face and the sector angle is defined as the angle between Q and the in-plane ⟨110⟩ direction.

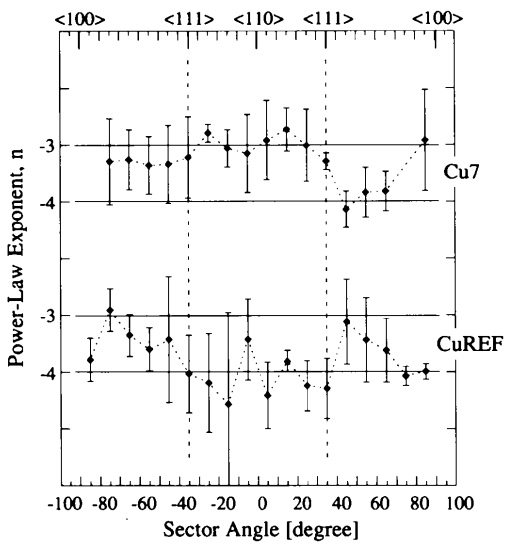

Fig. 11. Power-law exponent, n, as a function of sector angle for the Cu7 (top) and CuREF (bottom) net measurements in the low-Q configuration. Crystallographic directions contained in the Q plane of measurement are shown at the top of the figure, with two vertical dashed lines at ±35° (⟨111⟩ directions) drawn as an aid to the eye. The solid horizontal lines denote power-law exponents of -3 and -4 for each data set. Sector averages for CuREF were determined after subtraction of 0.006 cm^{-1} sr^{-1}, the measured incoherent scattering cross section. The averages were determined over an angular width about each sector angle of ±25°. Some data have been omitted because of poor statistics.

were calculated by subtracting the radially averaged CuREF cross section. This procedure does not completely subtract the $1/Q^4$ behavior at low-Q sector angles perpendicular to the deformed-sample surface-scratch direction. The observed low-Q power law will accordingly shift toward -4. The intermediate-Q data are not expected to be affected by the anisotropic surface scattering because, as Fig. 3 demonstrates, the difference between perpendicular and parallel sector averages is negligible above $Q \simeq 0.15\,\mathrm{nm}^{-1}$. The effect of the anisotropic surface scattering for a given sample should then be noticeable as a difference in the two sector curves.

The agreement between the two Cu54 curves is very good. A modest difference exists over sector angles between -65 and $-85°$ that can be traced to scratches on one side of the sample that run in the $+15°$ direction. The difference at $+20°$ can also be explained by these scratches. The other scratch direction for this sample was $-25°$ and did not result in a noticeable effect.

The two scratch directions for Cu35 were perpendicular. In this case, subtraction of the radially averaged CuREF cross sections is corrected for all directions. The two Cu35 sector-averaged curves in Fig. 9 are more or less consistent with this, although unexplained differences exist at the $\pm 75°$ sector angles.

The two scratch directions for Cu16 were parallel to within 15° and aligned with the $-55°$ sector direction. The direction orthogonal to this is the $+35°$ $\langle 111\rangle$, where the low-Q power-law exponent is seen to be shifted to a more negative value relative to the intermediate-Q result. The corresponding $1/Q^2$ amplitude in Table 3 is therefore not given.

The two scratch directions for Cu7 were also perpendicular and the sector-averaged data are not expected to be affected by the surface scattering. The CuREF case, previously discussed in association with Fig. 3, is one with the surface scratches aligned parallel to the $-10°$ sector angle. With the present data, it is not possible to determine if the CuREF sector data are affected by surface scattering.

Although surface scratches affect the data in an observable manner, it is important to note that the modulation in power-law exponent with sector angle for Cu54, Cu35 and Cu16 is not a result of the associated anisotropy. This is demonstrated further in the next subsection when the calculated dislocation scattering response is compared to the measured behavior.

(*d*) *Numerical calculations*

Equation (4) was numerically integrated to verify the measured sector averages presented in Figs. 9 and 11. The 12 individual $\{111\}\langle 110\rangle$ f.c.c. slip systems were explicitly accounted for in the calculation by determining the 12 values of φ and τ at each sector angle (direction of Q). Cross sections were calculated by summing the scattering response from the 12 slip systems as a function of Q for fixed values of L_0 and L^*. The power-law exponents at a given sector angle, or Q direction, were then determined. The Cu54 sector averages measured in the intermediate-Q configuration are compared to the calculated averages in Fig. 12. Both the $1/Q^2$ resonant behavior and the $1/Q^3$ orientation average behavior are verified by the numerical calculation, as is modulation between these behaviors as the sector angle is varied, respectively, between high- and low-symmetry directions of the single crystal. These calculations were performed over a Q range of $0.0655 \le Q \le 0.34\,\mathrm{nm}^{-1}$ with $L_0 = 5$ nm and $L^* = 50$ nm. Oscillations in the Bessel function were smoothed out by averaging over a flat distribution of pile-up widths, $25 \le L^* \le 75$ nm. In addition, a 5° φ and τ convolution was performed to include the effect of crystal mosaicity.

Some type of L_0 and L^* distribution is present in the deformed samples. The width of these distributions, as well as the nominal L_0 and L^* values, will depend on the amount of deformation and on the slip-system orientation relative to the deformation axis. The purpose of the numerical integration of (4) is not to determine the appropriate L_0 and L^* parameters for each sample – these will be obtained by transmission electron microscopy and published elsewhere – instead, the calculation presented in Fig. 12 demonstrates that the observed variation in scattering behavior with the deformed sample crystallographic direction can be modeled with realistic values of L_0 and L^*.

(*e*) *Dislocation densities*

An investigation of the scattering response of dislocations on individual slip planes is facilitated by the sector-averaged methodology presented above. The $1/Q^2$ amplitudes in the two $\langle 111\rangle$ directions contained in the

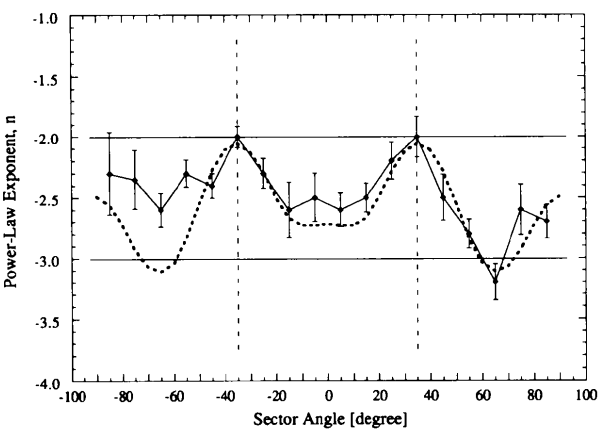

Fig. 12. Comparison of measured (solid line) and calculated (dotted line) sector averages. The measured averages are for Cu54 measured in the intermediate-Q configuration. The calculation represents a numerical integration of (4) with $L_0 = 5$ nm and $L^* = 50$ nm (see text).

measured Q plane have been listed separately in Table 3. In principle, these amplitudes are a function of the dislocation density on the corresponding {111} planes. However, the theoretical derivation developed by Seeger does not explicitly include the dislocation density. Modifications of (4) to include the dislocation density directly are not attempted here.

Although dislocation densities on the specific slip planes cannot currently be obtained from the $1/Q^2$ amplitudes, these data do contain information. The two {111} planes with a directional normal in the measured Q plane (and therefore directly examined in the measurement) are actually in the ⟨110⟩ deformation zone axis, as illustrated in Fig. 10. The corresponding $1/Q^2$ amplitudes for Cu54, Cu35 and Cu16 are resolvable, indicating that these planes are significantly populated by dislocations at the higher levels of deformation. By contrast, the $1/Q^2$ behavior in either ⟨111⟩ direction is not resolved in the Cu7 sample, indicating a lack of critical resolved shear stress on the associated {111} planes. The onset of the $1/Q^2$ response therefore identifies the condition in which the resolved shear stress rises above the yield point, creating dislocations in the process. In the present case, this condition is between 7 and 16% thickness reduction.

In principle, the shear stress on the two {111} planes in the deformation-direction zone axis (and therefore parallel to the compression axis) should be zero for all levels of deformation strain. (In other words, these slip systems have vanishing Schmid factors.) However, friction between the sample surface and the steel plates during deformation added a stress component perpendicular to the compression direction. Combined, the frictional and compressive forces could have induced yield on these {111} planes in Cu16, Cu35 and Cu54.

Bulk-averaged edge dislocation densities can be obtained from the $1/Q^3$ amplitudes listed in Table 3 for each sample by applying the result of Atkinson & Hirsch (1958),

$$\mathrm{d}\Sigma(Q)/\mathrm{d}\Omega = [(1-2\nu)/(1-\nu)]^2 \times \left(\pi a^2 b^2/2\kappa^2\right)\left(\rho_D/Q^3\right), \qquad (6)$$

where ρ_D is the edge dislocation density and all other quantities are as defined previously. To arrive at this result, Atkinson & Hirsch used first-order isotropic linear elasticity theory to describe the edge dislocation strain field. The small-angle scattering response from screw dislocations and dislocation cores was found to be a second-order effect (Atkinson & Hirsch, 1958). The edge dislocation density for each deformed sample is listed in Table 4. The additional density given for Cu7 was obtained from the radially averaged $1/Q^3$ response. The following copper material constants in (6) were used: $a = 0.77 \times 10^{-12}$ cm, $\nu = 0.34$, $b = 0.255$ nm and $\kappa = 0.01176$ nm^3.

Table 4. *Edge dislocation densities in deformed single-crystal copper measured by SANS*

Sample	ρ_D ($\times 10^{10}$ cm^{-2})
Cu7	0.9 (1) [0.57 (1)]
Cu16	1.9 (1)
Cu35	3.1 (1)
Cu54	5.2 (2)

The edge dislocation densities derived from these measurements can be compared with the results of other investigations of deformed copper. As part of an investigation of dynamic recovery, Staker & Holt (1972) deformed polycrystalline copper to a tensile strain of 10% at room temperature and studied the resulting dislocation substructure with transmission electron microscopy. They found that the dislocations were arranged in a cellular structure with an average dislocation density of approximately 1×10^{10} cm^{-2}.

Kopetskiy, Kulesko & Kokhanchik (1973) rolled single-crystal copper at room temperature to various degrees of thickness reduction. One set of samples had (110) faces and was rolled in the [1$\bar{1}$2] direction. This rolling geometry is similar to the compressional deformation employed in the current study; both had thickness reductions in the [110] direction. Kopetskiy *et al.* (1973) found extended dislocation tangles, closed loops and dipoles at low strain values (10 to 20%). At the higher levels of strain, however, the dislocation substructure became more uniform. Dislocation densities determined with transmission electron microscopy were 8×10^9 cm^{-2} and 1.1×10^{11} cm^{-2} at thickness reductions of 22 and 75%, respectively.

Ungár, Mughrabi, Rönnpagel & Wilkens (1984) investigated the X-ray line broadening induced by [100] tensile deformation of single-crystal copper. This type of deformation created a very heterogeneous dislocation arrangement. As part of their methodology, Ungár *et al.* were able to determine local dislocation densities, both at cell wall and cell interior locations. In general, the cell-wall density was found to be a factor of ten higher than the cell-interior density. Dislocation densities are given as a function of applied stress only. From an earlier publication (Mughrabi, Ungár & Wilkens, 1983), however, the axial strain at one stress value stress is given. Using this information, Ungár *et al.* (1984) found the total dislocation density (volume averaged over the cell-wall and cell-interior locations) at a strain of approximately 25% to be 2×10^{10} cm^{-2}.

With this brief and incomplete review of previous work under consideration, the edge dislocation densities obtained in this investigation seem reasonable, although, at the highest level of deformation (Cu54), the value may be somewhat low. To first order, the SANS response of edge dislocations will dominate, and this is one possible explanation for the low densities: the total density, including screw dislocations, will be higher. A

second explanation is the strain-compensation effect of edge dislocations on adjacent glide planes (dislocation dipoles) and in cell walls. If significant numbers of edge dislocations are in dipole and cell-wall configurations, the effective edge dislocation density measured with SANS will be reduced.

This work was supported by the National Science Foundation under Grant No. DMR-9213867. It is also based upon activities supported by the National Science Foundation under Agreement No. DMR-9122444. The support of the National Institute of Standards and Technology, US Department of Commerce, in providing the facilities used in this experiment is gratefully acknowledged. The assistance of Dr William Orts of the National Institute of Standards and Technology in using the SANS instrument is greatly appreciated. The author also expresses his gratitude to Dr Helmut Kaiser, University of Missouri, Research Reactor Center, for his translation of selected German results. Finally, the author is grateful to Drs John King and George Summerfield, University of Michigan, Department of Nuclear Engineering, for their interest during very useful discussions.

References

ATKINSON, H. H. (1959). *J. Appl. Phys.* **30**, 637–645.
ATKINSON, H. H. & HIRSCH, P. B. (1958). *Philos. Mag.* **3**, 213–228.
CHRIST, J. (1964). *Phys. Status Solidi*, **7**, 557–576.
GEROLD, V. & KOSTORZ, G. (1978). *J. Appl. Cryst.* **11**, 376–404.
HAMMOUDA, B., KRUEGER, S. & GLINKA, C. J. (1993). *J. Res. Natl Inst. Stand. Technol.* **98**, 31–44.
HIRTH, J. P. & LOTHE, J. (1982). *Theory of Dislocations*, p. 771. New York: Wiley.
KETTUNEN, P. O., LEPISTÖ, T., KOSTORZ, G. & GÖLTZ, G. (1981). *Acta Metall.* **29**, 969–972.
KOPETSKIY, CH. V., KULESKO, G. I. & KOKHANCHIK, L. S. (1973). *Fiz. Metal. Metalloved.* **35**, 624–631.
LEPISTÖ, T. K., KOSTORZ, G., KUOKKALA, V.-T. & KETTUNEN, P. (1991). *Mater. Sci. Eng.* **A131**, 171–176.
MUGHRABI, H., UNGÁR, T. & WILKENS, M. (1983). *Scr. Metall.* **17**, 797–805.
POROD, G. (1982). *Small-Angle X-ray Scattering*, edited by O. GLATTER & O. KRATKY, pp. 17–51. New York: Academic Press.
SCHMATZ, W. (1975). *Riv. Nuovo Cimento*, **5**, 398–422.
SCHMATZ, W., DEDERICHS, P. H. & SCHEUER, H. (1974). *Z. Phys.* **270**, 337–341.
SEEGER, A. K. (1959). *J. Appl. Phys.* **30**, 629–637.
STAKER, M. R. & HOLT, D. L. (1972). *Acta Metall.* **20**, 569–579.
UNGÁR, T., MUGHRABI, H., RÖNNPAGEL, D., WILKENS, M. (1984). *Acta Metall.* **32**, 333–342.